

**Fiscal Year 2011 Director's Strategic Initiative Final Report
Heterogeneous Device Architectures Incorporating Nitride
Semiconductors for Enhanced Functionality of
Optoelectronic Devices**

**by Anand V. Sampath, Meredith L. Reed, Michael Gerhold,
and Michael Wraback**

ARL-TR-6870

March 2014

NOTICES

Disclaimers

The findings in this report are not to be construed as an official Department of the Army position unless so designated by other authorized documents.

Citation of manufacturer's or trade names does not constitute an official endorsement or approval of the use thereof.

Destroy this report when it is no longer needed. Do not return it to the originator.

Army Research Laboratory

Adelphi, MD 20783-1197

ARL-TR-6870

March 2014

Fiscal Year 2011 Director's Strategic Initiative Final Report Heterogeneous Device Architectures Incorporating Nitride Semiconductors for Enhanced Functionality of Optoelectronic Devices

Anand V. Sampath, Meredith L. Reed, and Michael Wraback
Sensors and Electron Devices Directorate, ARL

Michael Gerhold
U.S. Army Research Office

REPORT DOCUMENTATION PAGE			Form Approved OMB No. 0704-0188		
<p>Public reporting burden for this collection of information is estimated to average 1 hour per response, including the time for reviewing instructions, searching existing data sources, gathering and maintaining the data needed, and completing and reviewing the collection information. Send comments regarding this burden estimate or any other aspect of this collection of information, including suggestions for reducing the burden, to Department of Defense, Washington Headquarters Services, Directorate for Information Operations and Reports (0704-0188), 1215 Jefferson Davis Highway, Suite 1204, Arlington, VA 22202-4302. Respondents should be aware that notwithstanding any other provision of law, no person shall be subject to any penalty for failing to comply with a collection of information if it does not display a currently valid OMB control number.</p> <p>PLEASE DO NOT RETURN YOUR FORM TO THE ABOVE ADDRESS.</p>					
1. REPORT DATE (DD-MM-YYYY) March 2014		2. REPORT TYPE DSI		3. DATES COVERED (From - To) October 2011–September 2013	
4. TITLE AND SUBTITLE Fiscal Year 2011 Director's Strategic Initiative Final Report Heterogeneous Device Architectures Incorporating Nitride Semiconductors for Enhanced Functionality of Optoelectronic Devices			5a. CONTRACT NUMBER		
			5b. GRANT NUMBER		
			5c. PROGRAM ELEMENT NUMBER		
6. AUTHOR(S) Anand V. Sampath, Meredith L. Reed, Michael Gerhold, and Michael Wraback,			5d. PROJECT NUMBER		
			5e. TASK NUMBER		
			5f. WORK UNIT NUMBER		
7. PERFORMING ORGANIZATION NAME(S) AND ADDRESS(ES) U.S. Army Research Laboratory ATTN: RDRL-SEE-M 2800 Powder Mill Road Adelphi, MD 20783-1197			8. PERFORMING ORGANIZATION REPORT NUMBER ARL-TR-6870		
9. SPONSORING/MONITORING AGENCY NAME(S) AND ADDRESS(ES)			10. SPONSOR/MONITOR'S ACRONYM(S)		
			11. SPONSOR/MONITOR'S REPORT NUMBER(S)		
12. DISTRIBUTION/AVAILABILITY STATEMENT Approved for public release; distribution unlimited.					
13. SUPPLEMENTARY NOTES * Army Research Office, ATTN: RDRL-ROE-L, P.O. Box 12211, Research Triangle Park, NC 27709-2211					
14. ABSTRACT Heterogeneous devices combine dissimilar materials with complementary device functionalities to achieve new functionalities that may provide revolutionary advances in technology. In these novel devices the physics and engineering of the interface of the dissimilar materials plays a critical role and requires considerable research. While nitride semiconductors have had great success as materials for sources and detectors of electromagnetic radiation across the spectrum from the ultraviolet (UV) to terahertz, heterogeneous integration of these materials with others having different spontaneous polarization, different crystal structure or a new functionality hold promise for devices with improved performance. This report discusses research efforts on two representative examples, III-Nitride/silicon carbide (SiC) avalanche photodetectors and compositionally inhomogeneous indium gallium nitride (InGaN) terahertz sources. Specifically, we demonstrate the efficacy of using III-Nitride semiconductors to improve the quantum efficiency (QE) of a photodetector employing a SiC-based gain region over a wide spectral range from 240 to 365 nm by overcoming surface states and weak absorption that limit the QE of homogenous SiC-based photodetectors in the deep UV and near UV regions, respectively. Furthermore, we have observed enhanced terahertz generation due to large internal in-plane electric fields in heteroepitaxially grown semi-polar and nonpolar GaN thin films due to the presence of self-assembled zincblende inclusions in an otherwise wurtzite crystal structure.					
15. SUBJECT TERMS III-Nitride Semiconductors, Silicon Carbide, Ultraviolet detectors, Terahertz Sources, Heterogeneous devices					
16. SECURITY CLASSIFICATION OF:			17. LIMITATION OF ABSTRACT UU	18. NUMBER OF PAGES 42	19a. NAME OF RESPONSIBLE PERSON Anand V. Sampath
A. Report Unclassified	b. ABSTRACT Unclassified	c. THIS PAGE Unclassified			19b. TELEPHONE NUMBER (Include area code) (301) 394-0104

Contents

List of Figures	iv
Acknowledgments	vi
1. Polarization-Enhanced III-Nitride-SiC Avalanche Photodiodes	1
1.1 GaN/SiC SAM-APDs.....	4
1.2 AlGaIn/AlN/SiC APDs.....	8
2. Fiber Laser Pumped Terahertz Radiation Sources Based on Inhomogeneous InGaIn Containing Zincblende Domains	14
2.1 Material Growth	15
2.2 Terahertz Source.....	17
3. References	25
Publications, Presentations, and Transitions	28
Distribution List	33

List of Figures

Figure 1. Spectral response of a homogeneous 4H-SiC APD (grey) and possible peak response shift for a III-Nitride-SiC APD.	2
Figure 2. Measured photoresponse of a 4H-SiC p-n ⁻ -metal photodetector.	3
Figure 3. Device structure of a III-Nitride/SiC APD.	5
Figure 4. Measured dark current (black), photocurrent (red), and gain (green) for a GaN/SiC APD. Temperature dependent I-V characteristics (inset).	5
Figure 5. Measured responsivity of GaN/SiC APDs (open shapes), typical response from a GaN detector (black), and the calculated response of a SiC detector through a GaN filter.	7
Figure 6. Cross-section of Al _x Ga _{1-x} N/AlN/SiC <i>n-i-p</i> photodetectors.	8
Figure 7. Left Axis: DC photoresponse of Al _{0.6} Ga _{0.4} N/SiC photodiode with no AlN barrier layer at 10 and 20 V. Gray dashed line is normalized response of homogeneous SiC <i>p-i-n</i> photodiode. Right Axis: Transmission of Al _{0.6} Ga _{0.4} N layer.	9
Figure 8. DC photoresponse of Al _x Ga _{1-x} N/AlN/SiC photodiodes with (a) 10-nm AlN barrier and (b) 120-nm barrier at various bias voltages. The dotted line in (a) and (b) is the normalized responsivity and measured responsivity of a homogeneous SiC <i>p-i-n</i> photodiode, respectively.	10
Figure 9. Modulated responsivity of Al _x Ga _{1-x} N/AlN/SiC photodiodes with (a) 10- and (b) 120-nm-thick AlN barrier layers.	11
Figure 10. Schematic of in-plane electric field due to stacking faults in nonpolar or semipolar nitride material.	14
Figure 11. AFM image showing excellent surface morphology of the <i>a</i> -plane GaN buffer layer grown by MBE.	16
Figure 12. X-ray diffraction data showing <i>a</i> -plane In _x Ga _{1-x} N with x~5–9% on a GaN buffer layer atop <i>r</i> -plane sapphire.	16
Figure 13. (a) Schematic of nonpolar InGaN rotation relative to the emitted terahertz polarization directions. Image plots of time-resolve (b) <i>s</i> - and (c) <i>p</i> -polarized terahertz waveforms from <i>a</i> -plane InGaN excited with 400 nm.	17
Figure 14. Sample rotation angle dependence of the peak <i>s</i> - and <i>p</i> -polarized terahertz emission (at t=0 shown in figure 6) from <i>a</i> -plane InGaN grown on <i>r</i> -plane sapphire.	18
Figure 15. Terahertz emission from <i>a</i> -plane InGaN (red curve) compared with that from <i>c</i> -plane InGaN (black curve) under identical excitation conditions.	19
Figure 16. Peak p-polarized terahertz signal dependence on excitation energy from high SF-density and SF-free m-plane GaN. Inset: Time-resolved terahertz waveforms from the SFD = 1- × 10 ⁶ -cm ⁻¹ sample at various excitation energies.	20
Figure 17. Plot of (a) p- and (b) s-polarized time-resolved terahertz radiation at θ = 0° and 180° and θ = 90° and 270°, respectively, from the SFD = 1 × 10 ⁶ -cm ⁻¹ m-plane GaN sample at 3.54, 3.44, and 3.35 eV excitation.	21

Figure 18. Azimuthal angle dependence of p- and s-polarized terahertz signal at t_0 from the SFD = $1 \times 10^6 \text{ cm}^{-1}$ sample at 3.54, 3.44, and 3.35 eV excitation and from SF free m-GaN at 3.44eV.	22
Figure 19. (a) Calculated band structure and carrier wavefunctions. (b) Azimuthal angle dependence of p-polarized terahertz signal at t_0 from the SFD = $1 \times 10^6 \text{ cm}^{-1}$ and SF-free samples at 3.44 eV ex-citation. The n=1 Fourier component has been removed. The solid line is calculated for bulk m-face wurtzite GaN.	23

Acknowledgments

The investigators would like to acknowledge members of the Nitride Semiconductor Optoelectronics Team with the Sensor and Electron Devices Directorate for their contributions to this research program: Dr. Gregory Garrett (Nitride/Oxide laser technical lead, optical studies of Oxide/Nitride LDs), Dr. Grace Metcalfe (terahertz sources technical lead, optical studies of indium gallium nitride [InGaN] materials), Dr. Paul Shen (technical consultation), Mr. Ryan Enck (molecular beam epitaxy [MBE] growth), Dr. Chad Gallinat (MBE growth), Dr. Nathaniel Woodward (optical evaluation of InGaN terahertz sources), Mr. Stephen Kelley (Device Fabrication). We also would like to acknowledge Professor Winston Schoenfeld's research group at the University of Central Florida for the development of oxide semiconductors as well as Professor Joe Campbell's group at the University of Virginia for the fabrication and some characterization of the GaN/silicon carbide avalanche photodetectors. We also thank Robert Ferrell and Professor Jim Speck of the University of California at Santa Barbara for providing the InGaN cell material employed in the active window solar cell.

1. Polarization-Enhanced III-Nitride-SiC Avalanche Photodiodes

Semiconductor-based ultraviolet (UV) avalanche photodetectors (APDs) have significant promise for reducing the size, weight, power requirements, and cost of Army systems for biological agent detection and/or identification, UV communications, and hostile fire detection. While photomultiplier tube (PMT) detectors have high sensitivity and low dark counts, these devices are susceptible to damage from shock as well as exposure to ambient light, very expensive (greater than \$500.00), inherently broad band, and require a high-voltage power supply.

In contrast, UV-APDs can be more rugged, compact, have reduced power supply requirements, and a lower cost. Commercially available silicon (Si) APDs benefit from a mature material system, easy integration, and a favorable impact ionization coefficient ratio (β/α ratio), which results in a very low excess noise factor ($k=\alpha/\beta=0.02$). However, the dark current of these devices in linear mode operation can be too high for certain applications, such as bio-fluorescence detection. In addition, the broadband sensitivity of Si from long-wavelength UV to the near infrared (IR) can impair systems that target a relatively narrow spectral band, therefore requiring elaborate filters. Moreover, high-sensitivity, commercially available, single photon counting avalanche photodiodes are not specified for operation at wavelengths shorter than 400 nm.

Silicon carbide (SiC) has many advantageous material qualities for realizing high gain, low noise, and low-dark current UV APDs, including a wide band gap, a large β/α ratio, and high quantum efficiency (QE). SiC APDs have been demonstrated with high quantum efficiency (60% at $\lambda=268$ nm), low dark current ($J_{\text{dark}}=64$ nA/cm² at a gain of 1000, which indicates primary dark current of less than 10 fA), excellent spatial uniformity (standard deviation less than 5% at gain of 5000 across active area), and low noise ($k=0.10$) (1–2). Near zero bias, these devices have achieved record detectivity of 4.1×10^{14} cmHz^{1/2}W⁻¹ at 270 nm, higher than for PMTs, Si detectors, and conventional charge-coupled device arrays, and, in Geiger-mode, single photon detection efficiency as high as 30% at room temperature (3–4). Despite this success, the response of 4H-SiC APDs is characterized by an abrupt decrease at wavelengths shorter than 260 nm, as well as a more gradual drop at long-wavelength between 320 and 370 nm; these spectral ranges are important for bio-chemical agent identification by fluorescence-free Raman spectroscopy and the detection of bio-fluorescence excited by 280-nm sources, respectively. The short-wavelength response is hindered by the inefficient collection of carriers generated by high-energy photons in the heavily doped top layer, which are trapped by surface states or recombine due to the short diffusion length of minority carriers (1). The long-wavelength tail results from weak indirect absorption extending to the bandgap of 4H-SiC at 3.23 eV ($\lambda \sim 380$ nm).

III-Nitrides are a family of direct band gap semiconductors that is tunable from the UV (200 nm) to the IR (1800 nm) by varying the alloy composition from aluminum nitride (AlN) (6.1 eV) to

gallium nitride (GaN) (3.4 eV) to indium nitride (InN) (0.69 eV). As a result, the III-Nitrides are a promising material for realizing high QE photodetectors with tunable response throughout the UV spectrum. While GaN UV photodetectors with QE greater than 50% have been demonstrated (5–6), APDs employing these alloys are hindered by materials issues. As a result, GaN APDs remain in their infancy, with performance vastly inferior to that of SiC devices (7). Furthermore, the significantly larger breakdown field of AlN over SiC (approximately 6 times) implies that aluminum gallium nitride (AlGaN)-based deep UV (DUV)-APDs would operate at significantly larger reverse bias than comparable SiC devices.

In contrast, integration of III-Nitride semiconductors with 4H-SiC can leverage the benefits of each material system to realize highly sensitive avalanche photodetectors throughout the UV spectral range (figure 1). In the near UV spectral range, where homogenous SiC APDs suffer from poor absorption, separate absorption and multiplication APDs (SAM-APDs) employing a GaN absorption region and a SiC multiplication region allows the possibility of having high QE owing to the direct band gap of GaN, as well as low dark current and high gain associated with the high quality SiC. In addition, this device structure benefits from the formation of a type II heterojunction with both the conduction and valence band energies of the GaN below those of the SiC and conduction band and valence band offsets that are between -0.6 and -0.9 eV and 0.7 and 1 eV, respectively (8). This band alignment promotes hole injection and inhibits electron injection from GaN into SiC, enabling single carrier injection of the photo-generated holes in the absorbing region into the SiC multiplication layer that is optimal since the hole ionization coefficient of SiC is much greater than that of the electron. Combined with the spatial separation of the absorption and multiplication regions, these devices may have lower noise than SiC APDs.

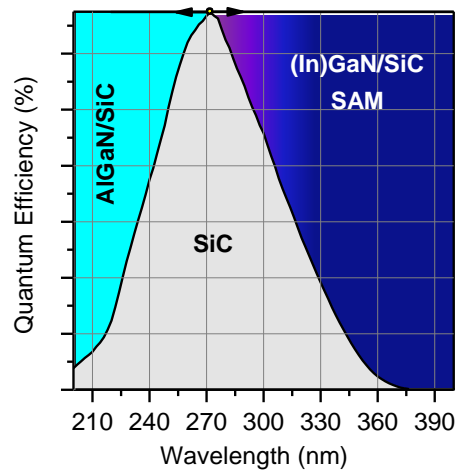


Figure 1. Spectral response of a homogeneous 4H-SiC APD (grey) and possible peak response shift for a III-Nitride-SiC APD.

In the DUV spectral range, the response of homogeneous SiC APDs suffer from increasing absorption and carrier generation in the top doped layer of the device, the short diffusion length of minority carriers in this region and the presence of a high density of surface states. During this program we have demonstrated a high DUV QE of approximately 40% at 200 nm in a SiC p-n⁻ -metal structure, where a thin transparent metal contact replaces the top n-doped layer of a conventional structure (figure 2). This improvement is attributed to the increased collection of carriers created by absorption of photons in this spectral range within the depletion region of the device where the photogenerated carriers are more effectively collected by drift despite the presence of surface recombination (9). However, as the metal contact is only approximately 50% transparent across the spectral range of interest, this approach limits the unity gain QE of the APD and therefore its potential single photon detection efficiency. In contrast, employing an n-type AlGa_N contact layer that is transparent throughout the spectral range of interest can eliminate these losses.

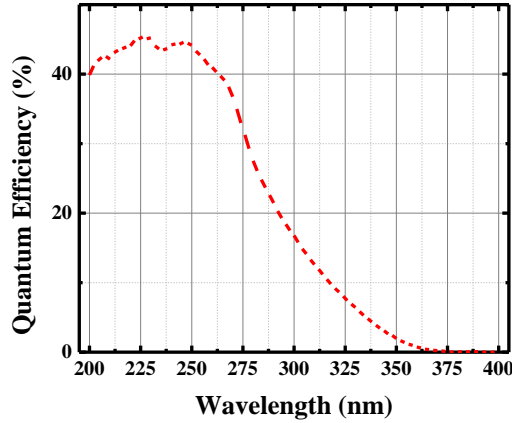


Figure 2. Measured photoresponse of a 4H-SiC p-n⁻ -metal photodetector.

These heterogeneous integrations are achieved by heteroepitaxial growth of the III-Nitride device layers by plasma-assisted molecular beam epitaxy on SiC epitaxial layers grown on 4H-SiC substrates. While heteroepitaxial growth of III-Nitrides on SiC substrates has been demonstrated previously, it is important to appreciate that the functional role of SiC in these structures beyond that of a substrate. The requirement for efficient carrier injection across these heterointerfaces introduces interesting challenges that are unlike traditional heterojunction APDs such as indium gallium arsenide/indium phosphorous (InGaAs/InP) telecommunications devices, including differences in spontaneous polarization, as well as lattice mismatch that have important implications for device performance.

As these detectors employ polar materials, with the spontaneous polarization of the Al_xGa_{1-x}N alloy increasing with AlN mole fraction and greater than that of SiC, a positive polarization

charge is expected at the hetero-interface between a III-polar $\text{Al}_x\text{Ga}_{1-x}\text{N}$ and SiC. For a GaN/SiC SAM APD structure, this charge can achieve an optimal electric field profile, a high field in the multiplication region of the structure desirable for high gain, and a low field within the absorption region, but insufficient or excessive charge can lead to poor performance. As a result, an additional method for controlling the density of interface charge is desirable. The presence of a larger density of polarization charge at the more strongly polar AlGaN/SiC interface can potentially further reduce the loss of carriers generated by DUV photons to interface states.

Furthermore, InGaAs/InP APDs benefit from lattice matching of these materials as well as the ability to epitaxially grow the InP multiplication region and InGaAs absorption region directly on an InP substrate without interruption at the heterointerface; in this manner the formation of deleterious defects can be prevented. In contrast, GaN has a 3.4% lattice mismatch with 4H-SiC that reduces with AlN mole fraction, resulting in the formation of threading dislocations that can act as leakage paths that increase dark current and prevent avalanche breakdown. While various heteroepitaxial buffer schemes have been developed for the growth of III-Nitrides on SiC, these approaches must be modified or preferably avoided since the SiC region is not simply a substrate, and the success of these devices hinges upon the efficient carrier injection across the heterointerface.

Finally, the constituents of each material act as dopants in the other material so that intermixing at the interface can play an important role on the performance of these devices.

1.1 GaN/SiC SAM-APDs

GaN/SiC SAM APDs were fabricated employing a 2- μm -thick p^+ -SiC layer, a 480-nm-thick n^- -SiC multiplication region doped to $5 \times 10^{15} \text{ cm}^{-3}$, a 15-nm-thick magnesium (Mg)-doped GaN p-type interface charge control layer (PICCL), a 300–500 nm thick, unintentionally doped, GaN absorption region and capped with a thin 10-nm-thick n^+ -GaN layer so as to minimize absorption in this region. This device structure takes advantage of the positive polarization charge at the GaN/SiC heterointerface to obviate the need for a n-type SiC charge layer while employing the Mg-doped GaN layer to control the magnitude of the interface charge for optimal performance. The GaN regions of these devices were deposited directly on the Si-face 4H-SiC structure by plasma-assisted molecular beam epitaxy at a substrate temperature of 850 °C. Immediately prior to growth, the epilayer surface is cleaned in-situ by periodically covering the surface with Ga metal and then allowing the metal to desorb. After wafer cleaning, mesas of various dimensions were defined using inductive coupled plasma dry etching in an argon and chlorine gas mixture (Ar/Cl_2). A SiC sidewall bevel angel of approximately 7° was formed to prevent premature edge breakdown. A 290-nm-thick silicon dioxide (SiO_2) layer, which acted as both a passivation layer and an antireflective coating, was deposited by plasma-enhanced chemical vapor deposition. The p- and n-type contacts were formed by electron beam evaporation of titanium/nickel (Ti/Ni). A drawing of the device structure is shown in figure 3.

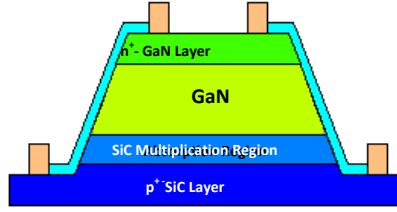


Figure 3. Device structure of a III-Nitride/SiC APD.

Figure 4 shows the voltage dependence of the dark current, photo current, and photomultiplication gain for a 250- μm -diameter device. The device demonstrated dark current less than 1 pA for bias up to 90% of the breakdown voltage. The device-area and temperature dependence of the dark current were studied to determine the dominant component of the dark current. The dark current was fitted to the gain in the range of 3–10 (reverse bias voltage of 148 V approximately 151 V) for devices with diameters of 250, 180, and 130 μm . The multiplied dark current was proportional to the device area rather than the perimeter, an indication that the primary dark current is due to bulk leakage. Dark current densities were calculated to be between 1.0 approximately 1.5 nA/cm^2 . This result suggests that the reverse leakage currents in these devices are limited by the SiC multiplication region despite the presence of threading dislocations at the heterointerface. It is also important to note that the dark current in these devices is approximately 1000 times lower than what has been observed for GaN APDs despite having areas that are up to approximately 25 times larger (7).

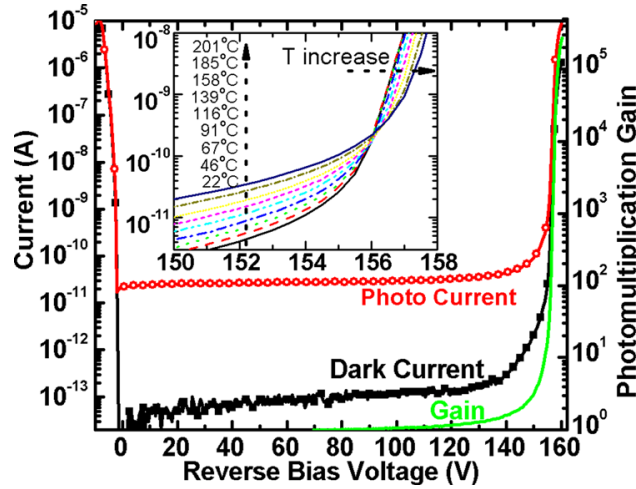


Figure 4. Measured dark current (black), photocurrent (red), and gain (green) for a GaN/SiC APD. Temperature dependent I-V characteristics (inset).

The inset of figure 4 shows the dark current of a 250- μm -diameter device at temperatures from room temperature to 201 $^{\circ}\text{C}$. A positive temperature dependence of the breakdown voltage was observed, an indication that breakdown is caused by avalanche multiplication. The breakdown voltage temperature coefficient was approximately 0.05 $\text{V}/^{\circ}\text{C}$. From Arrhenius plots of current in the voltage range of between 140 and 150 V low activation energies of approximately 0.1 eV were determined. This may indicate high levels of shallow level traps, which could be the result of high defect densities at the GaN/SiC interface.

The photocurrent was measured while the device was illuminated by a broad-spectrum xenon (Xe) UV lamp. The photomultiplication gain was calculated by dividing the photoresponse at a given voltage by the unity gain photoresponse. Here the unity gain was arbitrarily chosen at 70 V reverse bias where the photocurrent is relatively independent of voltage. We note that the calculated gain based on the reported impact ionization coefficients (10) is less than 1.05 at 70 V for this structure. A maximum gain greater than 10^5 was observed before the photocurrent reached the compliance current (1 μA) at reverse bias of 160 V.

The spectral responsivity was measured by comparing the response of the device under test with a calibrated Si reference photodiode. A Xe lamp and monochromator were used as the narrow spectrum light source from 300 to 400 nm. Figure 5 shows the measured responsivity versus wavelength at several voltages (open points). The spectral response at bias less than approximately 150 V is characterized by a local maxima at approximately 374 nm and a local minima at 366 nm that is neither consistent with the collection of carriers generated in the GaN absorption region nor with the response of a simple SiC APD. Modeling accounting for the GaN absorption (black solid line) and the response of a wholly SiC detector indicates that the peak at 374 nm is due to the reduced absorption in the GaN region resulting in more light passing through the GaN layer and reaching the SiC layer, indicating that the photoresponse is from the collection of carriers generated directly in the SiC multiplication region with the GaN absorption layer acting as an optical filter (blue dash line). The lack of GaN related response at low bias voltage is likely due to the confinement of the electric field within the SiC multiplication region and the concomitant low probability of photogenerated holes diffusing through the highly defective GaN/SiC interface to the SiC multiplication region. For bias below 90 V, there is almost no change of the responsivity, indicating that there is no gain in the SiC multiplication layer.

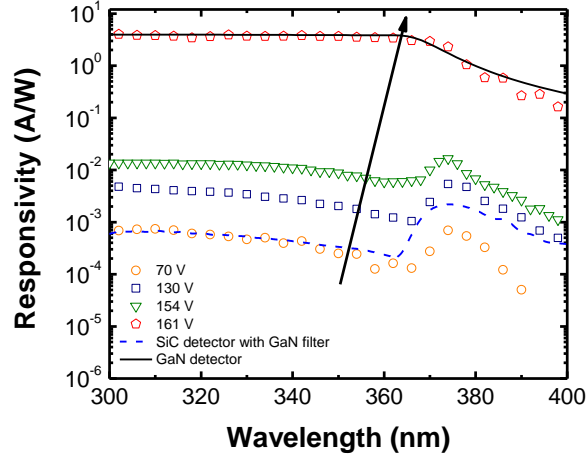


Figure 5. Measured responsivity of GaN/SiC APDs (open shapes), typical response from a GaN detector (black), and the calculated response of a SiC detector through a GaN filter.

The responsivity starts to increase for bias about 130 V, but the spectral shape remains unchanged until the bias exceeds approximately 150 V (not shown), indicating that there is no injection of holes from the GaN region up to this point. Above 154 V, the device begins to exhibit photoresponse that is clearly associated with the collection of carriers generated in the GaN absorption region. This transition in the photoresponse is attributed to the punch through of the electric field into the GaN absorption region and its gradual rather than sharp depletion with increasing bias, leading to the sweepout of the photogenerated holes into the multiplication region. Finally, at 160 V, the spectra exhibit basically a GaN response. A peak responsivity of 4.2 A/W was achieved at a reverse bias of 160 V. The cut off wavelength of the responsivity shifted from approximately 380 nm at 70 V reverse bias to approximately 400 nm at 150 V. This responsivity is significantly larger than what has been reported for GaN APDs (2), and can be attributed to the larger gain achieved in the SiC multiplication region. It is important to note that the transition from SiC dominated response at low reverse bias to GaN dominated response at high bias indicates that the gain calculated from the difference between the dark and photo IV characteristics in figure 4 is not purely due to avalanche multiplication. This methodology does not account for the increased collection of carriers photo-generated within the GaN absorption region with the on-set of punch through.

1.2 AlGaN/AlN/SiC APDs

Figure 6 shows a schematic of the cross section of a typical heterogeneous AlGaN/AlN/SiC *n-i-p* device. Several parameters of the device structure have been varied to demonstrate the effect of polarization induced charge at the AlGaN-AlN and AlN-SiC interfaces on the response of these detectors, including the thickness of the AlN barrier layer and the composition of the $n\text{-Al}_x\text{Ga}_{1-x}\text{N}$ layers. The AlGaN/AlN/SiC *n-i-p* structure consists of a 2- μm -thick p^+ ($2 \times 10^{18} \text{ cm}^{-3}$)-SiC layer, a lightly doped ($5 \times 10^{15} \text{ cm}^{-3}$)-*i*-SiC layer, an AlN barrier layer, an $\text{Al}_x\text{Ga}_{1-x}\text{N}$ layer, and finally a n^+ ($\sim 1 \times 10^{18} \text{ cm}^{-3}$)- $\text{Al}_x\text{Ga}_{1-x}\text{N}$ contact layer. The thickness of the AlN barrier layer in this series is 0, 10, and 120 nm. The AlN mole fraction in the $\text{Al}_x\text{Ga}_{1-x}\text{N}$ layers is 0.6 for the devices with 0- and 10-nm AlN barriers and 0.8 for the device with the 120-nm barrier layer. The SiC epitaxial layers were grown on Si-face, *n*-type, 4H-SiC substrates. The III-polar $\text{Al}_x\text{Ga}_{1-x}\text{N}$ epitaxial layers were heteroepitaxially grown by plasma-assisted molecular beam epitaxy directly upon the SiC epitaxial layers. The epitaxial layers were fabricated into circular mesas with 250- μm -diameters and 7° beveled sidewalls. The *n*- $\text{Al}_x\text{Ga}_{1-x}\text{N}$ Ohmic contact consists of Ti 10 nm/Al 100 nm/Ni 30 nm/Au 50 nm while the *p*-SiC Ohmic contact consists of Ni 25 nm/Ti 35 nm/Al 100 nm/Ni 80 nm. A 200-nm-thick silicon oxide antireflection layer was deposited on all devices.

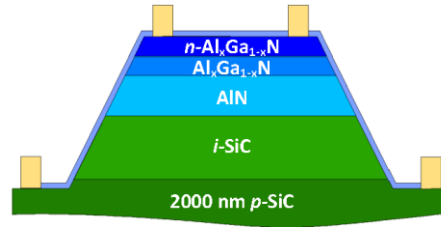


Figure 6. Cross-section of $\text{Al}_x\text{Ga}_{1-x}\text{N}/\text{AlN}/\text{SiC}$ *n-i-p* photodetectors.

The direct current (DC) and modulated (alternating current) photoresponse of the devices were measured by illuminating the devices with a laser-driven white light source passed through a monochromator. DC photocurrent measurements were taken with a Keithley 2400 source-measurement unit. The modulated characterization was conducted using a Stanford Research Systems 830 lock-in amplifier to measure the photocurrent generated by modulating the light source. A variable neutral density filter was used to keep the applied illumination power at 100 nW for all wavelengths.

The DC photoresponse of the photodiode without an AlN barrier layer is shown in figure 7. The shape of the spectral response is comparable to that of a homogeneous SiC *p-i-n* device, as shown by the normalized curve (dotted line), with peak responsivity occurring at approximately 275 nm. However, the short-wavelength response is more sharply cut-off at approximately 260 nm than the SiC *p-i-n* device. The measured photoresponse shows no bias dependence under 20 V,

indicating unity gain operation. In contrast, the DC photoresponse of the devices containing both the 10- and 120-nm AlN barrier layer, shown in figures 8a and b, show strong bias dependence and a red-shifting peak with increasing bias voltage. For the device containing the 10-nm barrier layer, the spectral response is characterized by a single peak at 260 nm at 10 V that increases and red-shifts until ultimately saturating at 275 nm around 14 V. The spectral shape of the response at reverse bias greater than 13 V is similar to that of the homogeneous SiC *p-i-n* diode with a peak response around 275 nm, but also with a strong short-wavelength cut off around 260 nm. By contrast, the response of the device with a 120-nm-thick barrier layer is characterized by a single peak around 226 nm at low bias voltages that moves to 242 nm with increasing bias. The short-wavelength cutoff in this device occurs at approximately 230 nm. In addition, the response at wavelengths longer than 260 nm is significantly suppressed over that of a homogenous SiC *p-i-n* diode (dotted line) at all bias voltages.

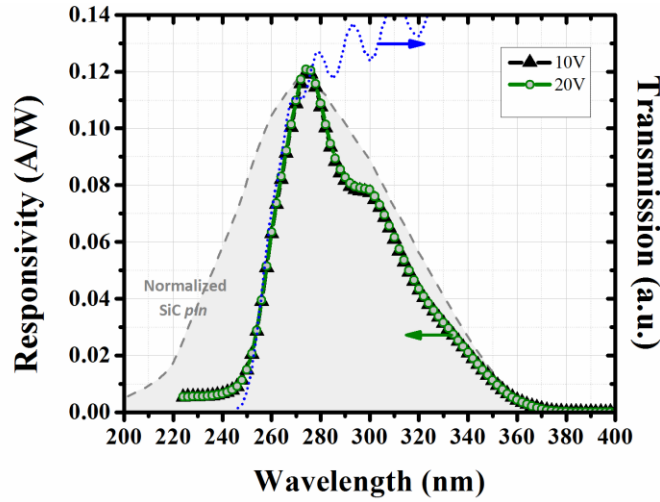


Figure 7. Left Axis: DC photoresponse of $\text{Al}_{0.6}\text{Ga}_{0.4}\text{N}/\text{SiC}$ photodiode with no AlN barrier layer at 10 and 20 V. Gray dashed line is normalized response of homogeneous SiC *pin* photodiode. Right Axis: Transmission of $\text{Al}_{0.6}\text{Ga}_{0.4}\text{N}$ layer.

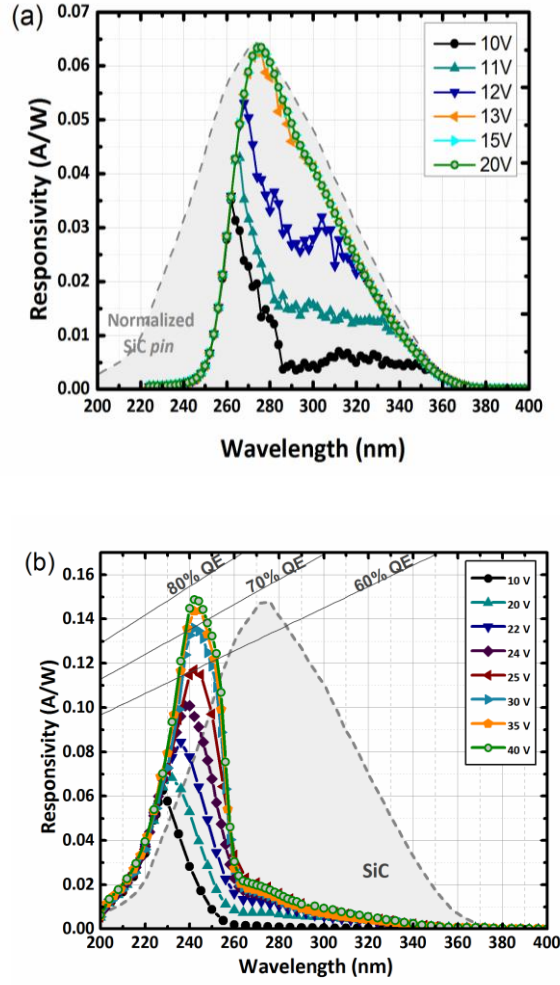


Figure 8. DC photoresponse of $\text{Al}_x\text{Ga}_{1-x}\text{N}/\text{AlN}/\text{SiC}$ photodiodes with (a) 10-nm AlN barrier and (b) 120-nm barrier at various bias voltages. The dotted line in (a) and (b) is the normalized responsivity and measured responsivity of a homogeneous SiC $p\text{-}i\text{-}n$ photodiode, respectively.

Figure 9 shows the modulated photoresponse of the devices with the 10- and 120-nm AlN barrier layer. For the device with the 10-nm barrier layer, the modulated response at 10 V consists of a peak at 260 nm in the in-phase component with a small quadrature component observed between 260 and 280 nm. Increasing the bias voltage results in an increase in the long-wavelength contribution centered at 275 nm. The long-wavelength response at 275 nm experiences a phase lag with respect to the 260 nm peak indicated by both the in-phase and quadrature contribution. For the device with the 120 nm barrier, the modulated response at 10 V consists of a peak at 226 nm in the in-phase component with positive in-phase and quadrature contributions observed at wavelengths longer than 226 nm. Increasing the reverse bias results in an increasing long wavelength contribution centered at 242 nm with positive in-phase and negative quadrature contributions.

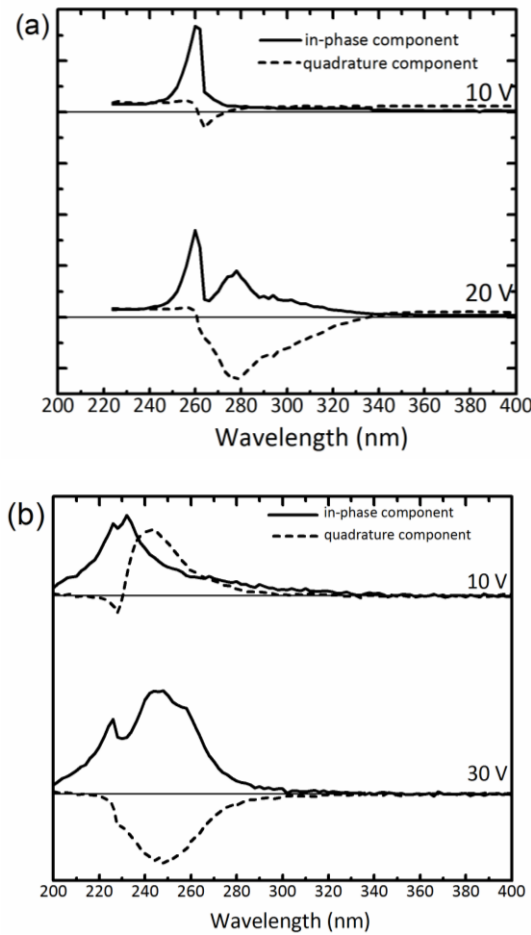


Figure 9. Modulated responsivity of $\text{Al}_x\text{Ga}_{1-x}\text{N}/\text{AlN}/\text{SiC}$ photodiodes with (a) 10- and (b) 120-nm-thick AlN barrier layers.

The spectral response in these diodes can be understood by considering the influence of the AlN barrier layer thickness, the composition of the $\text{Al}_x\text{Ga}_{1-x}\text{N}$ layers, and the energy band alignment between the Γ , L, and M valley minima of the 4H-SiC conduction band and the III-Nitride layers. For the detector without an AlN barrier, the top $\text{Al}_x\text{Ga}_{1-x}\text{N}$ layers do not contribute to the measured photoresponse due to the presence of a positive polarization induced interface charge at the $\text{Al}_x\text{Ga}_{1-x}\text{N}/\text{SiC}$ interface. As we have shown previously, this charge can be sufficiently large to prevent the punch-through of the electric-field into the $\text{Al}_x\text{Ga}_{1-x}\text{N}$ layer (11). As a result, carriers photogenerated in this region must rely on diffusion for collection and are lost to defect mediated recombination, resulting in the $\text{Al}_x\text{Ga}_{1-x}\text{N}$ layer acting as an optical filter cutting off the detector response at short-wavelengths. The measured photoresponse in figure 7 is therefore entirely associated with carriers generated in 4H-SiC. This conclusion is supported by the measured transmission of a similar 60% AlN mole fraction $\text{Al}_x\text{Ga}_{1-x}\text{N}$ film grown on a sapphire substrate that agrees well with the response cut-off observed for the diode (figure 7).

For the detector with the 10-nm AlN barrier, the presence of a large positive polarization-induced interface charge at the AlN/SiC interface and a large negative polarization-induced interface charge at the $\text{Al}_x\text{Ga}_{1-x}\text{N}/\text{AlN}$ interface results in a large dipole across the AlN barrier layer. Previous modeling of the band structure in this device indicates that this barrier is sufficient to block the transport of holes across the interface into the SiC (12). As a result, the top $\text{Al}_x\text{Ga}_{1-x}\text{N}$ layers again act as a short-wavelength optical filter since carriers generated in this region are lost to recombination. This argument is further supported by the agreement in short-wavelength cut-off in response between this device and the one without an AlN barrier layer.

Modeling also shows that electrons generated in the SiC region having sufficient energy can traverse the AlN barrier (12). Considering that the minimum transition energies between the Γ valley of the valence band and the M and L (indirect) and Γ (direct) valleys of the conduction bands of SiC are 3.25, 4.3, and 5.4 eV, respectively (13), the response observed at 10 V reverse bias in figure 3 can be explained by the transport and collection of electrons photogenerated in the L valley across the AlN barrier layer before they can relax to a lower valley within SiC. In this device, there are no electrons photoexcited to the higher energy Γ valley of SiC because of absorption in the $\text{Al}_{0.6}\text{Ga}_{0.4}\text{N}$ layer. The red-shift in response with increasing reverse bias is then associated with the concomitant lowering of the AlN barrier and higher field in the SiC that allows more efficient collection of lower energy electrons generated in the lower L and M valleys. At the highest biases investigated, the barrier to transport across the AlN is sufficiently reduced so that the long-wavelength response is consistent with that of a homogeneous *p-i-n* SiC diode.

Examination of the modulated photoresponse measurements as a function of reverse bias further supports this interpretation. The lack of a quadrature component in the response for wavelengths shorter than 265 nm at all reverse bias voltages suggests that these carriers have sufficient energy to traverse the barrier with minimum interaction. The presence of positive in-phase and negative

quadrature components in the photoresponse at 20 V reverse bias between 265 and 280 nm as shown in figure 9a indicates a phase lag due to the delay associated with the lowering of the barrier through the optical bias process. This occurs as photogenerated electrons in the SiC and holes in the $\text{Al}_x\text{Ga}_{1-x}\text{N}$ regions accumulate at the AlN/SiC and $\text{Al}_x\text{Ga}_{1-x}\text{N}/\text{AlN}$ interfaces, respectively, and partially cancel the polarization induced interface charge to lower the barrier.

Increasing the thickness of the AlN barrier layer to 120 nm and AlN mole fraction in the $\text{Al}_x\text{Ga}_{1-x}\text{N}$ layer to 0.8 increases the barrier height and promotes the absorption of high-energy photons in SiC, respectively. As a result, carriers are excited to the Γ or upper L valley and can traverse the barrier at low-bias voltages as shown in figure 8b by the peak response at approximately 225–230 nm. Modulated photoresponse measurements given in figure 9b show no quadrature component at wavelengths shorter than 226 nm, indicating that only these carriers are able to transport across the interface with minimal interaction with the barrier, further corroborating the increase in barrier height with increasing AlN thickness. The peak response shifts to approximately 242 nm with increasing reverse bias but the response at wavelengths longer than approximately 260 nm remains strongly suppressed at the highest biases investigated. This result is attributed to the significant barrier to electron transport that remains for electrons photogenerated in the lower L and M valleys. The modulated photoresponse measurements at 10 V bias reveal zero quadrature components at wavelengths shorter than approximately 230 nm, indicating that electrons photoexcited to the Γ valley are able to transport across the barrier layer with little interaction. Increasing the reverse bias to 30 V, the long wavelength contribution at 242 nm experiences a phase lag with respect to the peak at 225–230 nm, further supporting the conclusion that the lower energy peak results from the lowering of the barrier through both electrical and optical bias.

It should also be noted that the detector with a 120-nm AlN barrier and 80% $\text{Al}_x\text{Ga}_{1-x}\text{N}$ layer exhibits a peak QE of 76% at 242 nm, which is almost double that of the homogeneous SiC diode response, as shown by the dotted line in figure 8b. Owing to the transparency of the $\text{Al}_x\text{Ga}_{1-x}\text{N}$ and AlN at these wavelengths, this heterogeneous design enables the absorption of high-energy photons directly in the high-electric field SiC depletion region, resulting in an increase in the short-wavelength response. In contrast, these carriers are normally generated in the heavily doped top contact layer of a traditional homogeneous SiC device, resulting in poor collection efficiency. Analogously, the short-wavelength cut-off present in this heterogeneous detector is related to absorption in the wider band gap $\text{Al}_{0.8}\text{Ga}_{0.2}\text{N}$ layers, from which no photocurrent is collected due to the polarization induced barrier to transport.

This work demonstrates heterogeneous solar-blind $\text{Al}_x\text{Ga}_{1-x}\text{N}/\text{AlN}/\text{SiC}$ *n-i-p* photodetectors that enable the tailoring of the UV response of SiC. The large polarization induced interface charge occurring at the heterointerfaces is utilized to create a tunable barrier to electron transport across the heterointerface from the SiC to $\text{Al}_x\text{Ga}_{1-x}\text{N}$. This enables selective collection of electrons photoexcited into the Γ and L conduction band valleys of SiC, thereby tuning the spectral

response and improving the solar rejection. In addition, the short-wavelength response of SiC is improved by enabling absorption of high-energy photons in the SiC depletion region through the use of transparent $\text{Al}_x\text{Ga}_{1-x}\text{N}$ contact layers. A peak external quantum efficiency of 76% at 242 nm has been measured, which is nearly double that of conventional SiC *p-i-n* devices at this wavelength, and is attributed to suppression of the effects of surface states and absorption in heavily doped layers currently hindering homogeneous SiC devices.

2. Fiber Laser Pumped Terahertz Radiation Sources Based on Inhomogeneous InGaN Containing Zincblende Domains

Since the bandgap of AlN, GaN, and InN and its alloys spans the UV through IR wavelength range, III-Nitride-based terahertz devices can be engineered to operate at fiber-laser wavelengths for low-cost, compact, field-deployable terahertz systems leveraging fiber optic technology. These systems will have a number of applications including stand-off explosive detection and the ability to see through obscurants. Recently, we observed enhanced terahertz generation due to large stacking-fault (SF) related internal in-plane electric fields (figure 10) in *m*-plane GaN thin films (14). The SFs are thin zincblende inclusions in an otherwise wurtzite crystal structure and form due to heteroepitaxial growth of nonpolar GaN on lattice-mismatched substrates. The strong internal, in-plane polarization of the wurtzite crystalline structure is terminated at the wurtzite/zincblende interface, where charge accumulation leads to strong electric fields within the wurtzite domains that point in the same direction (along the *c*-axis of the crystal), effectively creating an array of contactless photoconductive (PC) switches. In-plane transport of carriers generated under ultrashort pulse excitation proceeds parallel to the electric field, leading to a terahertz radiation component polarized preferentially along this axis of the sample. The built-in field is estimated to be approximately 290 kV/cm in the wurtzite region of *m*-plane GaN with a SF density of approximately $1 \times 10^6 \text{ cm}^{-1}$.

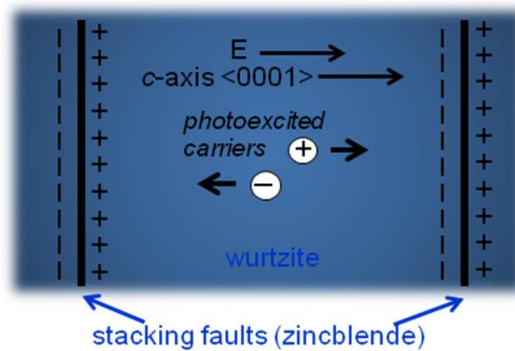


Figure 10. Schematic of in-plane electric field due to stacking faults in nonpolar or semipolar nitride material.

Because of built-in lateral SF-related fields, nonpolar and semipolar InN or InGaN are ideal as terahertz sources operating near fiber-laser wavelengths (1030 and 1550 nm). Recently, nonpolar InN was investigated and showed similar SF-related fields (15). Unfortunately, the best quality InN and high In-fraction InGaN still have high unintentional doping (UID) concentrations that can screen the terahertz field (16). Small In-concentration $\text{In}_x\text{Ga}_{(1-x)}\text{N}$ ($x < 0.3$), however, has a UID concentration low enough such that p -doping is possible. By using $\text{In}_x\text{Ga}_{(1-x)}\text{N}$ material with a bandgap engineered near 515 nm ($x \sim 0.26$), the doubled frequency of a compact femtosecond fiber laser could be used. We successfully developed a heterogeneous nitride-based terahertz source operating at 400 nm using U.S. Army Research Laboratory (ARL)-grown a -plane InGaN.

2.1 Material Growth

For efficient terahertz emission, a high density of SFs resulting from growth on lattice mismatched substrates is necessary. We achieved growth of a -plane InGaN epitaxial layers on double-sided polished r -plane sapphire using a Veeco Modular Gen II molecular beam epitaxy (MBE) reactor. High-quality growth of a -plane InGaN involves precise control over several growth parameters, including growth temperature and the relative arrival rate of group III and group V atoms to the surface. Although the growth conditions for c -plane InGaN material can serve as a guide, optimization must be performed for a -plane growth since In incorporation, ideal growth temperature, and growth kinetics change with crystal orientation.

Firstly, growth of single-crystal InGaN epitaxially on r -plane sapphire requires the development of a suitable nucleation material as well as an appropriate buffer layer material to ensure high-quality InGaN. Guided by the nucleation material used in c -plane growth, we grew an a -plane GaN buffer layer on either low-temperature (approximately 600 °C) grown GaN or high-temperature (approximately 800 °C) grown AlN. Characterization of the resulting films by atomic force microscopy (AFM) and double crystal x-ray diffraction revealed that growth on the low-temperature-grown GaN nucleation layer yielded a higher quality, lower surface roughness GaN buffer layer.

Next, we optimized the GaN buffer layer, which provides a low lattice mismatched surface for the growth of InGaN. The buffer layer deposition transitions from a three-dimensional growth mode to a two-dimensional step-flow growth through the coalescence of the nucleation sites at the sapphire-GaN interface (known as Stranski-Krastinov growth). The GaN buffer layer also isolates the InGaN epilayer from any oxygen that may diffuse from the sapphire substrate. Isolation of the InGaN from substrate surface contaminants and the effusion of oxygen is especially important for terahertz detection since screening effects due to the resulting background carriers will lower the terahertz detection efficiency. Deposition of the GaN buffer layer was optimized using a series of Ga flux and growth temperature adjustments and in situ monitoring using reflection high energy electron diffraction and pyrometer temperature measurements. A high-quality a -plane GaN buffer layer was ultimately obtained using a two-step growth process, a Ga flux of 2.1×10^{-7} Torr, and a thickness of 500 nm atop the low-

temperature-grown GaN nucleation layer to provide sufficient isolation from the sapphire substrate. Excellent surface morphology (surface roughness of 8.8 nm) of the GaN buffer was verified using AFM (figure 11).

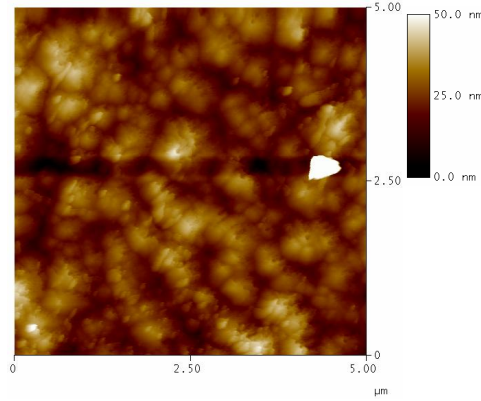


Figure 11. AFM image showing excellent surface morphology of the *a*-plane GaN buffer layer grown by MBE.

To determine the process window for the growth temperature of *a*-plane InGaN, we grew a series of samples, each at a lower substrate temperature until saturation of the In content occurred. We then adjusted the Ga flux to limit the In content to approximately 7.8% for a bandgap near 400 nm. Once we achieved saturation, the surfaces of these samples were compared to determine which growth temperature led to the smoothest surface. Once a determination was made on the relative Ga flux and growth temperature, a series of growths were performed to determine the minimum In flux necessary to grow stoichiometric InGaN without the accumulation of In droplets, which lead to droplet related defects. The highest quality *a*-plane InGaN films were grown at a temperature of 575 °C, a Ga flux of 1.8×10^{-7} Torr, and an Influx of 2.1×10^{-7} Torr. X-ray diffraction data of the film confirms an In concentration of approximately 5–9% (figure 12).

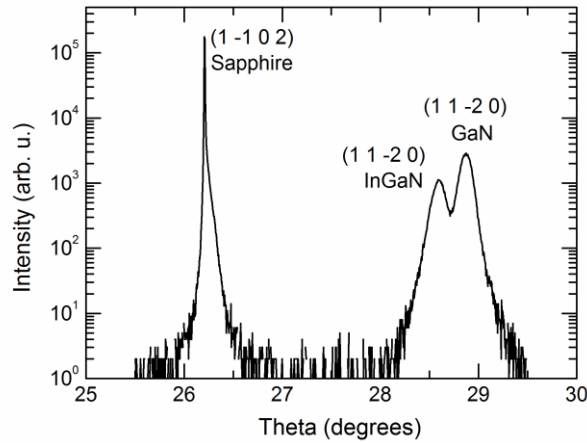


Figure 12. X-ray diffraction data showing *a*-plane $\text{In}_x\text{Ga}_{1-x}\text{N}$ with $x \sim 5\text{--}9\%$ on a GaN buffer layer atop *r*-plane sapphire.

2.2 Terahertz Source

When the ARL-grown a -plane InGaN films were used on r -plane sapphire, we achieved terahertz emission using ultrafast (approximately 150-fs pulse width) excitation at 400 nm. The pump source, incident on the sample at 45° to the surface normal, was obtained by frequency-doubling a 250-kHz Ti:Sapphire-pumped regenerative amplifier at 800 nm. The subsequent terahertz emission is collected with a pair of off-axis parabolic mirrors onto a zinc telluride (ZnTe) crystal for polarization sensitive electro-optic sampling. The terahertz source is mounted on a 360° rotation stage for sample rotation dependence measurements. Figure 13a illustrates the orientation of the terahertz source relative to the incident pump beam and collected s - and p -polarized terahertz radiation.

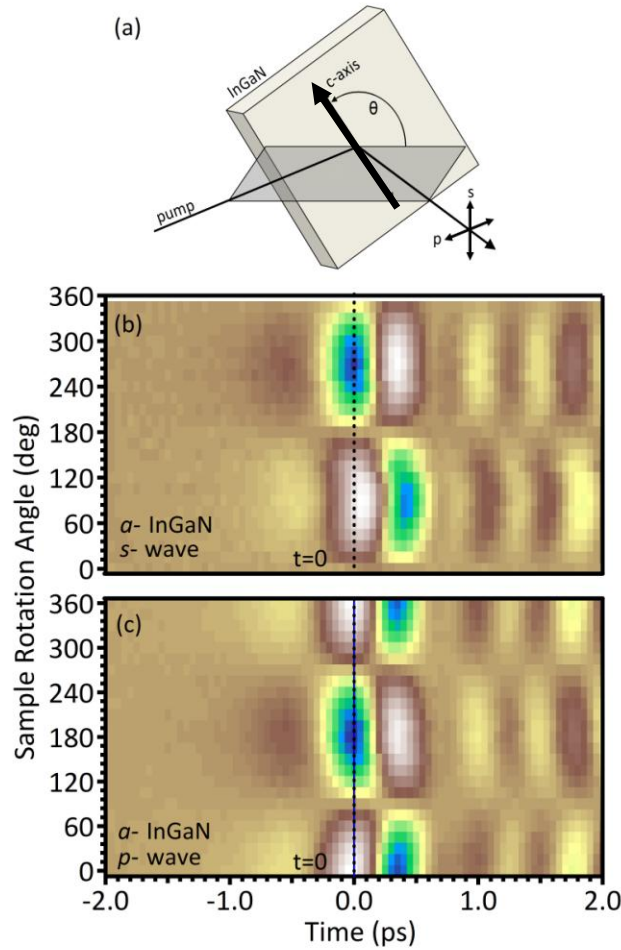


Figure 13. (a) Schematic of nonpolar InGaN rotation relative to the emitted terahertz polarization directions. Image plots of time-resolve (b) s -, and (c) p -polarized terahertz waveforms from a -plane InGaN excited with 400 nm.

The image plots in figures 13b and c show the time-resolved *s*- and *p*-polarized terahertz emission from *a*-plane $\text{In}_{0.15}\text{Ga}_{0.85}\text{N}$ as a function of sample rotation, respectively. The white areas denote positive values while the blue areas represent negative values. Several peaks associated with water absorption may also be seen to the right of the peak terahertz emission. A strong dependence on the rotation angle is observed in the image plots. To further analyze the sample rotation dependence of the *a*-plane InGaN, the terahertz signal at $t=0$ from the image plots in figure 13 is plotted in figure 14 as a function of sample rotation angle for both *s*- and *p*-polarizations. The data fit well to $\sin\theta$ and $\cos\theta$ functions, consistent with in-plane transport parallel to the *c*-axis direction due to SF-induced lateral electric fields. Optical rectification is neglected since it would appear as a $\sin(2\theta)$ dependence.

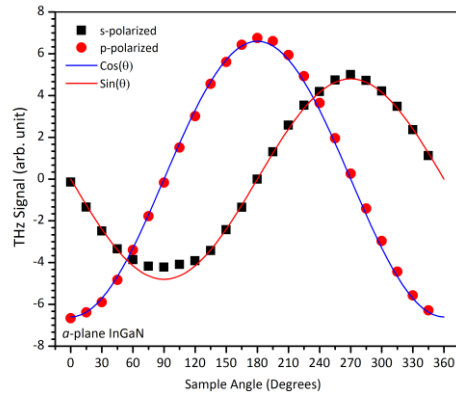


Figure 14. Sample rotation angle dependence of the peak *s*- and *p*-polarized terahertz emission (at $t=0$ shown in figure 6) from *a*-plane InGaN grown on *r*-plane sapphire.

For comparison, we plot in figure 15 the maximum terahertz emission from *a*-plane InGaN (red curve) against that from *c*-plane InGaN (black curve) under identical excitation conditions. With only initial material and SF density optimization of the *a*-plane InGaN, the terahertz emission from the nonpolar sample is already a factor of 2 larger than that from the *c*-plane InGaN. Terahertz emission from *c*-plane InGaN is attributed to the photo-Dember effect, which stems from the difference in the diffusion of photoexcited electrons and holes from the surface.

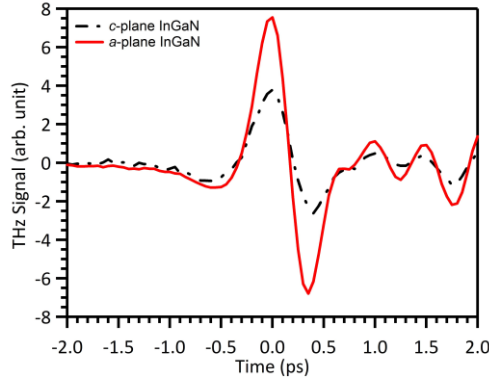


Figure 15. Terahertz emission from *a*-plane InGaN (red curve) compared with that from *c*-plane InGaN (black curve) under identical excitation conditions.

To further understand the significance of the SFs, we directly probe the quantum structures by tuning the ultrafast pulse excitation energy across the wurtzite GaN bandgap energy ($E_W=3.43$ eV at room temperature) and study the emitted terahertz radiation. Previous studies in nonpolar GaN at 5 K (17) directly correlated luminescence at 3.47 eV to the donor-bound exciton (D_0X) and below bandedge luminescence at 3.41 eV to SFs. Calculations showed that although no SF-related localized states exist in the bandgap, SFs can give rise to quantum-well-like regions of zincblende-like material embedded in the wurtzite lattice that can bind carriers, resulting in emission near 3.41 eV (18, 19). Furthermore, the internal electric fields along the polar (0001) direction resulting from the termination of the large internal polarization (20) at the zincblende/wurtzite interface are further manifested in lateral triangular potentials that add additional confinement (21, 22). Evidence of this large SF-related built-in lateral field was observed in the wurtzite regions of nonpolar nitride semiconductors from terahertz emission excited by femtosecond pulses (23, 24). However, the photon energy of the excitation pulses was significantly higher than the bandgap energy in these efforts, so effects near the zincblende inclusions were obscured.

We observe carrier localization and nonlinear susceptibility in polar lateral heterostructures in *m*-plane GaN observed through terahertz emission spectroscopy. We monitor the evolution of terahertz radiation generated from lateral carrier transport in the continuum just above the wurtzite bandgap to that from instantaneous polarization due to spatially separated electron-hole pairs bound to the potential wells associated with the stacking faults just below this bandgap. In addition, we observe subbandgap terahertz emission resulting from optical rectification due to the enhanced resonant nonlinear susceptibility stemming from the lateral heterostructure.

The samples consist of GaN epilayers grown on *m*-plane 6H-SiC substrates. The growth of these structures resulted in basal plane stacking faults in the *m*-plane GaN having predominantly I1 character. To create a range of SF-densities, the thin films were grown to a thickness of 262.5 nm using ammonia molecular beam epitaxy, 0.87 μm using metalorganic chemical vapor

deposition, and 20 μm using hydride vapor phase epitaxy, with a SF-density (average zincblende region spacing) of $3 \times 10^6 \text{ cm}^{-1}$ (3 nm), $1 \times 10^6 \text{ cm}^{-1}$ (10 nm), and $0.3 \times 10^6 \text{ cm}^{-1}$ (33 nm), respectively. The high SF-density materials were compared to an approximately 330 μm -thick SF-free m-GaN substrate from Mitsubishi Chemical Co., Ltd. The samples were optically excited using ultrafast pulses (approximately 150 fs) from the frequency-doubled tunable signal beam (350 nm–380 nm) of an optical parametric amplifier pumped by a 250 kHz regenerative Ti:sapphire amplifier at 800 nm. The p-polarized excitation beam was incident on the GaN sample at 45° to the surface normal, and the subsequent terahertz emission was collected with a pair of off-axis parabolic mirrors for polarization sensitive ZnTe-based electro-optic sampling. The terms p- and s-polarization refer to the polarization parallel and perpendicular to the plane of incidence, respectively. All measurements were taken at room temperature.

Figure 16 compares the excitation energy dependence of the peak p-polarized terahertz signal, normalized by the number of incident photons, from the high SF-density m-plane GaN films with that from the SF-free m-plane GaN substrate. The samples were oriented such that the c-axis was parallel to the plane of incidence. At a photon energy of 3.54 eV, above the wurtzite GaN bandgap, E_W , the high-SF samples have a significantly stronger terahertz signal than the SF-free sample, with the strength of the terahertz signal increasing as the SF density becomes larger. As the excitation energy decreases towards E_W , the terahertz emission from all GaN samples diminishes due in part to decrease in absorption with lower excitation energy. No terahertz emission is observed from the SF-free sample at excitations below E_W owing to negligible absorption. For the high SF-density samples, we observe not only subbandgap terahertz emission just below E_W but also an inversion of the terahertz waveform polarity as the excitation laser energy tunes across the wurtzite GaN bandgap (see inset in figure 16).

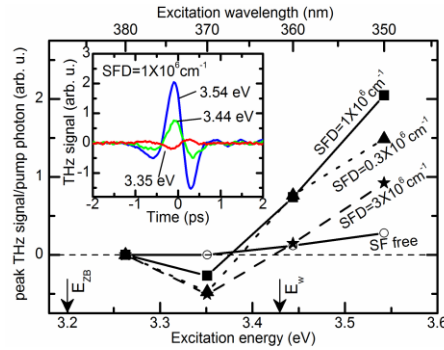


Figure 16. Peak p-polarized terahertz signal dependence on excitation energy from high SF-density and SF-free m-plane GaN. Inset: Time-resolved terahertz waveforms from the $\text{SFD} = 1 \times 10^6 \text{ cm}^{-1}$ sample at various excitation energies.

For more detailed analysis of the change in the terahertz generation mechanism, and, consequently, the variation in the carrier dynamics as the excitation energy approaches the bandgap of the zincblende inclusions in the m-plane GaN, we explore the dependence of the terahertz radiation on the azimuthal angle, θ , by rotating the sample about the surface normal. The emission from the SF-free sample exhibits no angular dependence, as expected for surface normal carrier transport resulting from the photo-Dember effect (25). The terahertz signal from the high SF-density materials, on the other hand, reveals a significant angular dependence. As an example, plots of the p- and s-polarized time-resolved terahertz waveforms at several azimuthal angles from the $1 \times 10^6 \text{ cm}^{-1}$ SF-density m-plane GaN for excitation centered at 3.54 eV (350 nm), 3.44 eV (360 nm), and 3.35 eV (370 nm) are displayed in figures 17a and b, respectively. At all excitation energies, the terahertz waveforms flip with a 180° azimuthal angle rotation and have about a 2-THz spectral distribution. For subwurtzite bandgap excitation, the waveforms are inverted relative to the above bandgap case. A slight phase shift of the subbandgap terahertz signal is also observed.

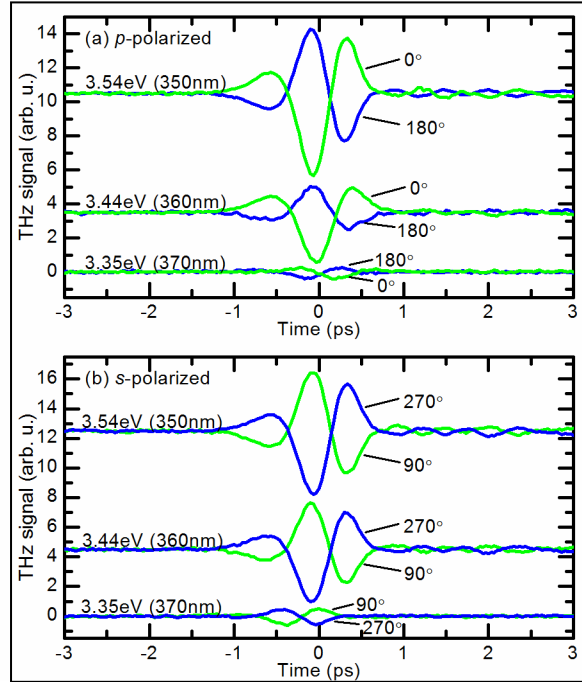


Figure 17. Plot of (a) p- and (b) s-polarized time-resolved terahertz radiation at $\theta = 0^\circ$ and 180° and $\theta = 90^\circ$ and 270° , respectively, from the $\text{SFD} = 1 \times 10^6 \text{ cm}^{-1}$ m-plane GaN sample at 3.54, 3.44, and 3.35 eV excitation.

Figure 18 plots the terahertz signal at a fixed time, t_0 , against the azimuthal angle. The time, t_0 , is taken at the first primary terahertz waveform maximum or minimum. For above bandgap excitation at 3.54 eV, the s- and p-polarized data are proportional to the functions $f_s(\theta) = \sin\theta$ and

$f_p(\theta) = -\cos\theta$, respectively. Terahertz emission due to nonlinear effects would also show a $\sin(n\theta)$ or $\cos(n\theta)$ component, where $n>1$ (25), which is clearly not observed for above bandgap excitation. Diffusion or intersubband transitions (26) cannot account for the angular dependence. The sinusoidal dependence, however, is similar to that observed by Metcalfe et al. (23) at 4.66 eV (266 nm) excitation and indicates linearly polarized terahertz emission associated with in-plane carrier transport in internal SF-related electric fields which point along the [0001] direction. A larger stacking fault density creates a smaller average spacing between the zincblende inclusions that terminate the polarization of the wurtzite matrix, leading to a larger electric field in the wurtzite material and therefore a higher peak terahertz signal with increasing SF density (figure 16). Rotation of the c-axis about the surface normal also rotates the internal electric field, and, consequently, the emitted terahertz polarization direction, leading to the sinusoidal dependence measured using the polarization-sensitive ZnTe detection crystal.

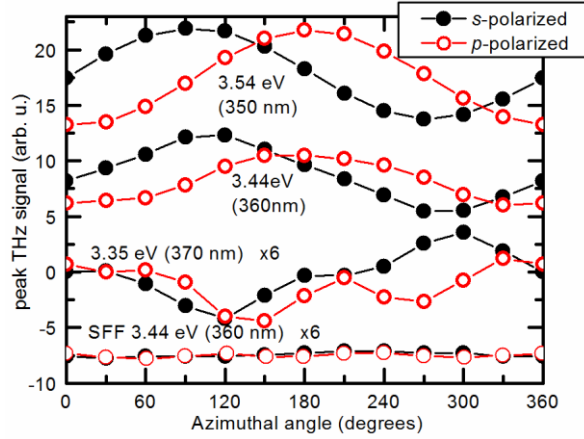


Figure 18. Azimuthal angle dependence of p- and s-polarized terahertz signal at t_0 from the $SFD = 1 \times 10^6 \text{ cm}^{-1}$ sample at 3.54, 3.44, and 3.35 eV excitation and from SF free m-GaN at 3.44 eV.

When the excitation energy is tuned below E_w , the azimuthal angle dependence of the terahertz emission from the high SF-density sample begins to alter. Although the dominant angular feature remains the $n=1$ component at 3.44 eV excitation energy, higher order oscillations ($n>1$) begin to appear that are much larger than those observed in the terahertz emission from the SF-free m-GaN material at the same excitation energy. At 3.35 eV excitation energy, below the wurtzite GaN bandgap, the polarity of the $n=1$ signal inverts and the higher order oscillations become more prominent. Insight into this behavior can be gleaned from figure 19a, which illustrates the calculated band structure and carrier wavefunctions in the potential created by the quantum-well-like zincblende inclusions within the wurtzite GaN matrix. Spatially separated electron-hole pairs generated by below wurtzite bandgap excitation create a dipole moment, which points opposite to the transport-induced dipole moment created by carriers excited into the continuum.

Although following the calculations by Metcalfe et al. (23) gives an estimated unscreened field in the zincblende regions of almost 3 MV/cm, the dipole moment of electron-hole pairs confined within the very thin inclusion layers ($<8 \text{ \AA}$) is insufficient to account for the subbandgap terahertz generation. However, the electron and hole wavefunctions extend significantly into the wurtzite matrix, with a dipole moment more characteristic of their center-to-center spacing (approximately 25 \AA), than the thickness (less than 8 \AA) of the zincblende inclusions. Since the strength of the terahertz emission increases with the extent of this dipole (27), we attribute the subbandgap terahertz polarity inversion of the $n=1$ angular component to the instantaneous polarization of these spatially separated electron-hole pairs localized within lateral quantum structure containing multiple crystal symmetries.

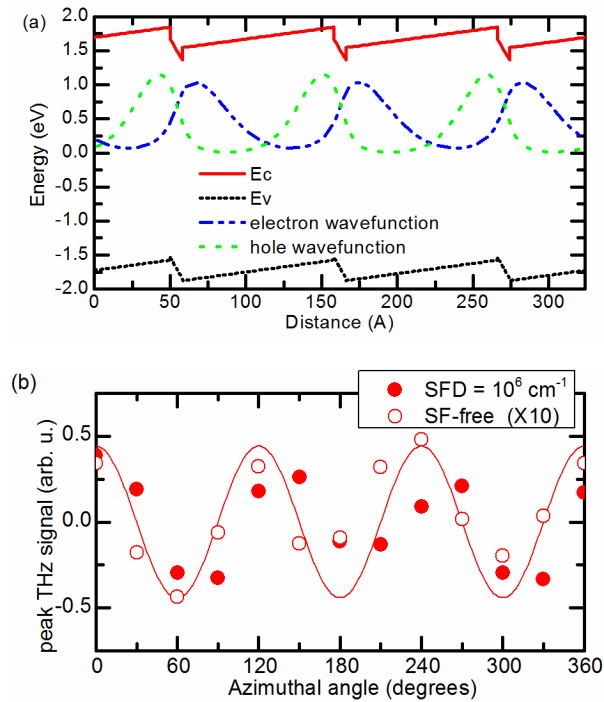


Figure 19. (a) Calculated band structure and carrier wavefunctions. (b) Azimuthal angle dependence of p-polarized terahertz signal at t_0 from the SFD = $1 \times 10^6 \text{ cm}^{-1}$ and SF-free samples at 3.44 eV ex-citation. The $n=1$ Fourier component has been removed. The solid line is calculated for bulk m-face wurtzite GaN.

The higher order oscillations suggest a nonlinear optical process. Terahertz generation due to optical rectification has been observed in various semiconductors, such as (100) and (111) InP, (111) InSb, (111) InAs, and a-plane InN (28–30) but typically at high pump fluences above the bandgap. However, there have been reports of subbandgap emission and polarity inversion of the terahertz waveform at near bandgap excitation in (111) bulk GaAs and InAs/GaAs superlattices (31, 32) due to optical rectification and the resonant behavior of the nonlinear susceptibility and

in (100) GaAs (33) due to the combination of a real photocurrent and virtual photoconductivity (34, 35). Furthermore, electric-field-biased quantum structures have demonstrated enhanced nonlinear susceptibility compared to their bulk counterparts (36, 37). A similar phenomenon is observed in the SF m-GaN shown in figure 18, for which the higher order oscillations ($n>1$) are much bigger than those in SF-free m-face GaN, indicating an enhanced nonlinear susceptibility in the lateral polar heterostructures created by the SF compared to that in bulk wurtzite GaN. We expect similar effects for a-plane and semipolar GaN. For c-plane GaN, the internal electric field and instantaneous polarization are along the surface normal direction so we would not expect to observe any angular dependence.

A further understanding of the nonlinear susceptibility associated with the higher order oscillations and its enhancement in the SF material with respect to that in the bulk SF-free m-GaN can be attained by removing the $n=1$ Fourier component and plotting the remaining data in conjunction with the calculated azimuthal angle dependence of the p-polarized terahertz signal due to optical rectification for a m-face wurtzite crystal structure (figure 19b). Since the (11-2) direction of the zincblende-like inclusions points along the m-direction (11-00) of the bulk wurtzite GaN, the calculation for the zincblende-like inclusions were on a (11-2) surface zincblende crystal. In both cases, the calculation shows a dominant 3θ component and much smaller $n=1$ component, with the solid line in figure 19b representing the calculated $n>1$ components for p-polarized terahertz. Similar results (not shown) were obtained for s-polarized terahertz. Moreover, it is clear that the nonlinear susceptibility alone cannot account for the subbandgap SF related terahertz signal, which shows a dominant $n=1$ feature. Comparison of the $n>1$ components of p-polarized terahertz at t_0 from the $\text{SFD} = 1 \times 10^6\text{-cm}^{-1}$ sample and SF-free sample at 3.44 eV excitation indicate that both samples show clear $n=3$ components, but the strength of the nonlinearity in the SF sample is enhanced by an order of magnitude relative to its SF-free counterpart (38).

3. References

1. Bai, X.; Guo, X.; McIntosh, D. C.; Liu, H.; Campbell, J. C. High Detection Sensitivity of Ultraviolet 4H-SiC Avalanche Photodiodes. *IEEE J. Quantum Electron.* **2007**, *43* (12), 1159–1162.
2. Guo, X.; Beck, A. L.; Li, X.; Campbell, J. C.; Emerson, D.; Sumakeris, J. Study of Reverse Dark Current in 4H-SiC Avalanche Photodiodes. *IEEE J. Quantum Electron.* **2005**, *41* (4), 562–567.
3. Liu, M.; Bai, X.; Hu, C.; Guo, X.; Campbell, J. C.; Pan, Z.; Tashima, M. M. Low Dark Count Rate and High Single-Photon Detection Efficiency Avalanche Photodiode in Geiger-Mode Operation. *IEEE Phot. Tech. Lett.* **2007**, *19*, 378–380.
4. Bai, X.; McIntosh, D.; Liu, H.; Campbell, J. C. Ultraviolet Single Photon Detection With Geiger-Mode 4H-SiC Avalanche Photodiodes. *IEEE Phot. Tech. Lett.* **2007**, *22*, 1822–1824.
5. Li, T.; Beck, A. L.; Collins, C.; Dupuis, R. D.; Campbell, J. C.; Carrano, J. C.; Schurman, M. J.; Ferguson, I. A. Improved Ultraviolet Quantum Efficiency Using a Semitransparent Recessed Window AlGaIn/GaN Heterojunction p-i-n Photodiode. *Appl. Phys. Lett.* **1999**, *75* (16), 2421–2423.
6. Biyikli, N.; Kartaloglu, T.; Aytur, O.; Kimukin, I.; Ozbay, E. High-Speed Visible-Blind GaN-Based Indium–Tin–Xide Schottky Photodiodes. *Appl. Phys. Lett.* **2001**, *79*, (17), 2838–2840.
7. Limb, J. B.; Yoo, D.; Ryou, J. H.; Lee, W.; Shen, S. C.; Dupuis, R. D.; Reed, M. L.; Collins, C. J.; Wraback, M.; Hanser, D.; Preble, E.; Williams, N. M.; Evans, K. *Appl. Phys. Lett.* **2006**, *89*, 011112.
8. Danielsson, E.; Zetterling, C. M.; Ostling, M.; Linthicum, K.; Thomson, D. B.; Nam, O. H.; Davis, R. F. The Influence of Band Offsets on The IV Characteristics for GaN/SiC Heterojunctions. *Sol. State Electron.* **2002**, *46*, 827–835.
9. Sampath, A. V.; Rodak, L. E.; Chen, Y.; Zhou, Q.; Campbell, J. C.; Shen, H.; Wraback, M. High Quantum Efficiency Deep Ultraviolet 4H-SiC Photodetectors. *Electron. Lett.* **2013**, *49*, 1629–1630.
10. Ng, B. K.; David, J.P.R.; Tozer, R. C.; Rees, G. J.; Yan, F.; Zhao, J. H.; Weiner, M. *IEEE T Electron Dev* **2003**, *50* (8), 1724–1732.
11. Sampath, A. V.; Zhou, Q. G.; Enck, R. W.; McIntosh, D.; Shen, H.; Campbell, J. C.; Wraback, M. *Appl. Phys. Lett.* **2012**, *101*, 093506.

12. Rodak, L. E.; Sampath, A. V.; Gallinat, C. S.; Chen, Y.; Zhou, Q.; Campbell, J. C.; Shen, H.; Wraback, M. *Appl. Phys. Lett.* **2013**, *103*, 071110.
13. Zollner, S.; Chen, J. G.; Duda, E.; Wetteroth, T.; Wilson, S. R.; Hilfiker, J. N. *J. Appl. Phys.* **1999**, *85*, 8353.
14. Metcalfe, G. D.; Shen, H.; Wraback, M.; Hirai, A.; Wu, F.; Speck, J. S. Enhanced Terahertz Radiation From High Stacking Fault Density Nonpolar GaN. *Appl. Phys. Lett.* **2008**, *92*, 241106.
15. Metcalfe, G. D.; Shen, H.; Wraback, M.; Koblmüller, G.; Gallinat, C.; Wu, F.; Speck, J. S. Terahertz Radiation From Nonpolar InN Due To Drift in an Intrinsic In-Plane Electric Field. *Appl. Phys. Express* **2010**, *3*, 092201.
16. Chern, G. D.; Readinger, E. D.; Shen, H.; Wraback, M.; Gallinat, C. S.; Koblmüller, G.; Speck, J. S. Excitation Wavelength Dependence of Terahertz Emission from InN and InAs. *Appl. Phys. Lett.* **2006**, *89*, 141115.
17. Liu, R.; Bell, A.; Ponce, F. A.; Chen, C. Q.; Yang, J. W.; Khan, M. A. *Appl. Phys. Lett.* **2005**, *86*, 021908.
18. Stampfl, C.; Van de Walle, C. G. *Phys. Rev. B* **57** **1998**, 15052 (1998) and references therein.
19. Rebane, Y. T.; Shreter, Y. G.; Albrecht, M. *Phys. Status Solidi A* **1997**, *164*, 141.
20. Iwata, H. P.; Oberg, S.; Briddon, P. R. *Materials Science Forum* **2004**, *457*, 1617.
21. Belabbes, A.; de Carvalho, L. C.; Schleife, A.; Bechstedt, F. *Phys. Rev. B* **2011**, *84*, 125108.
22. Bernardini, F.; Fiorentini, V.; Vanderbilt, D. *Phys. Rev. B* **1997**, *56*, R10024.
23. Betcalfe, G. D.; Shen, H.; Wraback, M.; Hirai, A.; Wu, F.; Speck, J. S. *Appl. Phys. Lett.* **2008**, *92*, 241106.
24. Metcalfe, G. D.; Shen, H.; Wraback, M.; Koblmüller, G.; Gallinat, C.; Wu, F.; Speck, J. S. *Appl. Phys. Express* **2010**, *3*, 092201.
25. Sakai, K. (ed.). *Terahertz Optoelectronics* (Springer, Berlin, 2005), pp. 1–27 and pp. 63–97.
26. Machhadani, H.; Tchernycheval, M.; Sakr, S.; Rigutti, L.; Colombelli, R.; Warde, E.; Mietze, C.; As, D. J.; Julien, F. H. *Phys. Rev. B* **2011**, *83*, 075313.
27. Turchinovich, D.; Jepson, P. Uhd; Monozon, B. S.; Koch, M.; Lamann, S.; Rossow, U.; Hangleiter, A. *Phys. Rev. B* **68** **2003**, 241307(R).
28. Chuang, S. L.; Schmitt-Rink, S.; Greene, B. I.; Saeta, P. N.; Levi, A.F.J. *Phys. Rev. Lett.* **1992**, *68*, 102.
29. Kono, S.; Gu, P.; Tani, M.; Sakai, K. *Appl. Phys. B: Lasers Opt.* **2000**, *71*, 901.

30. Ahn, H.; Ku, Y.-P.; Chuang, C.-H.; Pan, C.-L.; Lin, H.-W.; Hong, Y.-L.; Gwo, S. *Appl. Phys. Lett.* **2008**, 92, 102103.
31. Zhang, X.-C.; Jin, Y.; Yang, K.; Schowalter, L. J. *Phys. Rev. Lett.* **1992**, 69, 2303.
32. Zhang, X.-C.; Jin, Y.; Ware, K.; Ma, X. F.; Rice, A.; Bliss, D.; Larkin, J.; Alexander, M. *Appl. Phys. Lett.* **1994**, 64, 622.
33. Hu, B. B.; Zhang, X.-C.; Auston, D. H. *Phys. Rev. Lett.* **1991**, 67, 2709.
34. Yamanishi, M. *Phys. Rev. Lett.* **1987**, 59, 1014.
35. Yablonovitch, E.; Heritage, J. P.; Aspnes, D. E.; Yafet, Y. *Phys. Rev. Lett* **1989**, 63, 976; **1989**, 63, 1896 (E).
36. Tsang, L.; Ahn, D.; Chuang, S. L. *Appl. Phys. Lett.* **1988**, 52, 697.
37. Fejer, M. M.; Yoo, S.J.B.; Byer, R. L.; Harwit, A.; Harris, Jr., J. S. *Phys. Rev. Lett.* **1989**, 62, 1041.
38. Metcalfe, G. D.; Hirai, A.; Young, E. C.; Speck, J. S.; Shen, H.; Wraback, M. Terahertz Studies of Carrier Localization in Spontaneously Forming Polar Lateral Heterostructures. *Phys. Status Solidi Rapid Research Letters* **2013**, 7, DOI 10.1002/pssr.201308099 (2013).

4. Publications, Presentations, and Transitions

Refereed Papers (14 total) (4-FY11) (7- FY12) (3- FY13)

- Sampath, A. V.; Enck, R. W.; Shen, H.; Wraback, M.; Zhou, Q.; McIntosh, D.; Campbell, J. III-Nitride/SiC Separate Absorption and Multiplication Avalanche Photodiodes: The Importance of Controlling Polarization-Induced Interface Charge. *Int. J. of High Speed Electron. and Systems* **2011**, 20, 487.
- Sampath, A. V.; Zhou, Q.; Enck, R.; Gallinat, C. S.; Rotella, P.; McIntosh, D.; Shen, P.; Campbell, J.; Wraback, M. Impact of Hetero-Interface on the Photoresponse of GaN/SiC Separate Absorption and Multiplication Avalanche Photodiodes. *Proceedings of the 2011 International Semiconductor Device Research Symposium (ISDRS 2011)* DOI: 10.1109/ISDRS.2011.6135205, 2011.
- Shen, H. P.; Sampath, A. V.; Zhou, Q.; Campbell, J.; Wraback, M. Effect of Interface Polarization Charge on GaN/SiC Separate Absorption and Multiplication Avalanche Photodiodes. *ECS Transactions* **2011**, 41-6, 81.
- Zhou, Q.; McIntosh, D. C.; Lu, Z.; Campbell, J. C.; Sampath, A. V.; Shen, H.; Wraback, M. GaN/SiC Avalanche Photodiodes. *Appl. Phys. Lett.* **2011**, 99, 131110.
- Sampath, A. V.; Zhou, Q. G.; Enck, R. W.; McIntosh, D.; Shen, H.; Campbell, J. C.; Wraback, M. p-Type Interface Charge Control Layers for Enabling GaN/SiC Separate Absorption and Multiplication Avalanche Photodiodes. *Applied Physics Letters* **2012**, 101, 093506.
- Sampath, A. V.; Enck, R. W.; Gallinat, C. S.; Shen, H.; Wraback, M.; Zhou, Q.; McIntosh, D.; Campbell, J. C. III-Nitride/SiC Avalanche Photodetectors for Enabling Compact Biological Agent Identification and Detection. *Proceedings of SPIE*, **8376**, 83760O.
- Metcalf, G. D.; Gallinat, C. S.; Shen, H.; Wraback, M.; Wienecke, S.; Young, E. C.; Speck, J. S. Effects of Strain Relaxation on the Photoluminescence of Semipolar InGaN. *OSA CLEO Technical Digest* **2012**, JW3L.3.
- Rodak, L. E.; Sampath, A. V.; Gallinat, C. S.; Enck, R. W.; Smith, J.; Shen, H.; Wraback, M.; Chen, Y.; Zhou, Q.; Campbell, J. C. Aluminum Gallium Nitride/Silicon Carbide Separate Absorption and Multiplication Avalanche Photodiodes. *Proceedings of IEEE Lester Eastman Conference on High Performance Devices (LEC)*, 10.1109/lec.2012.6410993, 2012.

- Das, N. C.; Reed, M. L.; Sampath, A. V.; Shen, H.; Wraback, M.; Farrell, R.; Iza, M.; Cruz, S. C.; Lang, J. R.; Young, N. G.; Terao, Y.; Neufeld, C. J.; Keller, S.; Nakamura, S.; DenBaars, S. P.; Mishra, U. K.; Speck, J. S. Heterogeneous Integration of InGaN and Silicon Solar Cells for Enhanced Energy Harvesting. *Proceedings of the 38th IEEE Photovoltaic Specialists Conference*, 2012.
- Woodward, N. T. et al. THz Emission from a-plane InGaN, OSA CLEO *Technical Digest* **2012**, JW2A.57.
- Woodward, N. T. et al. Terahertz Sources Based on Polarization in Bulk InGaN Flms. *Proc. International Conference on Ultrafast Phenomena* 2012.
- Metcalf, G. D.; Hirai, A.; Young, E. C.; Speck, J. S.; Shen, H.; Wraback, M. Terahertz Studies of Carrier Localization in Spontaneously Forming Polar Lateral Heterostructures. *Phys. Status Solidi Rapid Research Letters*, 7, DOI 10.1002/pssr.201308099, 2013.
- Rodak, L. E.; Sampath, A. V.; Gallinat, C. S.; Chen, Y.; Zhou, Q.; Campbell, J. C.; Shen, H.; Wraback, M. Solar-Blind $\text{Al}_x\text{Ga}_{1-x}\text{N}/\text{AlN}/\text{SiC}$ Photodiodes With a Polarization-Induced Electron Filter. *Applied Physics Letters* **2013**, 103, 071110.
- Wei, M.; Boutwell, R. C.; Garrett, G. A.; Goodman, K.; Rotella, P.; Wraback, M.; Schoenfeld, W. V. Impact of Oxygen Source Parameters on Homoepitaxial ZnO Films Grown at Low-Temperature on Zn-Polar Substrates. *Journal of Alloys and Compounds* **2013**, 552, 127.
- Symposium/Conference Presentations (11- Total) (2- FY11) (8- FY12) (1- FY13) “Hybrid III-Nitride/SiC Ultraviolet Avalanche Photodiodes”, M. Wraback, A.V Sampath, R.W. Enck, H. Shen, Q. Zhou, D. McIntosh, and J. Campbell, invited presentation at the Workshop on Compound Semiconductor Materials and Devices”, Savannah, GA, February, 2011.
- “Effect of Interface Polarization Charge on GaN/SiC Separate Absorption and Multiplication Avalanche Photodiodes”, H. Shen, A. V. Sampath, Q. Zhou, J. Campbell, and M. Wraback, invited presentation at 2011 Electrochemical Society Meeting, Boston, MA.
- “Impact of Hetero-interface on the Photoresponse of GaN/SiC Separate Absorption and Multiplication Avalanche Photodiodes”, A.V Sampath, R.W. Enck, H. Shen, Q. Zhou, D. McIntosh, J. Campbell and M. Wraback, invited presentation at 2011 International Semiconductor Device Research Symposium, College Park, MD, December 2011.
- Garret, G. p-GaN/MgZno Optoelectronic Devices Grown on Bulk ZnO to be presented at the 48th Annual Workshop on Compound Semiconductor Materials and Devices, WOCSEMMAD 2012, February 19–22, Napa, CA.

Sampath, A. V. et al. III-Nitride/SiC Avalanche Photodetectors for Enabling Compact Biological Agent Identification and Detection. *SPIE Defense, Security and Sensing Symposium*, April 2012, Baltimore MD.

Woodward, N. T. Woodward et al. THz Emission From a-Plane InGaN. *Conference on Lasers and Electro-Optics (CLEO)*, San Jose, CA, May 2012.

Metcalfe, G.D; Gallinat, C. S.; Shen, H.; Wraback, M.; Wienecke, S.; Young, E. C.; Speck, J. S. Effects of Strain Relaxation on the Photoluminescence of Semipolar InGaN., *Conference on Lasers and Electro-Optics (CLEO)*, San Jose, CA, May, 2012.

Das, Naresh C.; Reed, Meredith I.; Sampath, Anand V.; Shen, H. Paul; Wraback, Michael; Farrell, R.; Iza, M.; Cruz, S. C.; Lang, J. R.; Young, N. G. Terao, Y.; Neufeld, C. J.; Keller, S.; Nakamura, S.; DenBaars, S. P.; Mishra, U. K.; Speck, J. S. Heterogeneous Integration of InGaN and Silicon Solar Cells for Enhanced Energy Harvesting. *Presented at the 38th IEEE Photovoltaic Specialists Conference*, Austin, TX, June 2012.

Woodward, N. et al. Terahertz Sources Based on Polarization in Bulk InGaN Films. *International Conference on Ultrafast Phenomena*, Lausanne, Switzerland, July 2012.

Rodak, L. E. et al. Aluminum Gallium Nitride/Silicon Carbide Separate Absorption and Multiplication Avalanche Photodiodes. *Lester Eastman Conference on High Performance Devices*, Providence, RI 2012. **Best poster paper award winner**

Rodak, L.; Sampath, A. V.; Gallinat, C. S.; Shen, H.; Wraback, M.; Chen, Y.; Zhou, Q.; Campbell, J. C. A III-Nitride Polarization Enhanced Electron Filter for Controlling the Spectral Response of Solar-blind $\text{Al}_x\text{Ga}_{1-x}\text{N}/\text{AlN}/\text{SiC}$ Photodiodes. *presented at the 10th International Conference on Nitride Semiconductors*, National Harbor, MD, August 2013.

Reports (3- Total) (1 – FY12) (2- FY13)

Metcalfe, G. D.; Woodward, N. T.; Shen, H.; Wraback, M.; Hsu, P. S.; Speck, J. Photoreflectance and Strain Relaxation Studies of Semipolar InGaN. *Bulletin of the American Physical Society*, BAPS.2013.MAR.Y23.4 (2013).

Sampath, Anand V.; Reed, Meredith L.; Gerhold, Michael; Wraback, Michael FY11 DSI - Heterogeneous Architectures Incorporating Nitride Semiconductors for Enhanced Functionality of Optoelectronic Devices (FY11); TR-5902, 2012.

Das, N. C.; Reed, M. L.; Sampath, A. V.; Shen, H.; Wraback, M.; Farrell, R. M.; Iza, M.; Cruz, S. C.; Lang, J. R.; Young, N. G.; Terao, Y.; Neufeld, C. J.; Keller, S.; Nakamura, S.; Denbaars, S. P.; Mishra, U. K.; Speck, J. S. Anti Reflection (AR) Coating for Indium Gallium Nitride (InGaN) Solar Cells; ARL-TR-6124;U.S. Army Research Laboratory: Adelphi, MD, 2012.

Briefings/Seminars (6- Total) (1-FY11) (3- FY12) (2-FY13)

Sampath, A. V.; Enck, R. W.; Shen, H.; Zhou, Q.; McIntosh, D.; Campbell, J.; Wraback, Michael. III-Nitride/SiC Separate Absorption and Multiplication Avalanche Photodiodes. *invited* seminar at West Virginia University, Morgantown, WV, October, 2011.

Wraback, M. Polarization Enhanced Wide Bandgap Semiconductor Optoelectronics”, *invited* seminar at the University of Notre Dame, South Bend, IN, April, 2012.

Metcalfe, G. D. “THz Materials, Devices and Applications,” *SEDD/CISD Science Day*, Adelphi, MD, April 2012.

Metcalfe, G. D. “THz Materials, Devices and Applications,” *Technical Assessment Board (TAB) review*, Adelphi, MD, May 2012.

Wraback, M. “Optoelectronic Applications of Interest to the Army Utilizing AlGaIn Films”, *invited* presentation at the ARO/ARL Workshop on Growth of High Quality AlGaIn Films, Adelphi, MD, January, 2013

Wraback, M. “Polarization Enhanced Wide Bandgap Semiconductor Optoelectronics”, *invited* seminar at the National Institute of Standards and Technology (NIST), Gaithersburg, MD, July, 2013.

Patent Awards (2) /Applications (1)

Wraback, M. et al. “Polarization Enhanced Avalanche Photodetector and Method Thereof”, U.S. Patent 8,269,223

Shen, H. et al. “Semiconductor Photodetector with Transparent Interface Charge Control Layer and Method Thereof”, U.S. Patent 8,269,222

Shen, Paul H.; Sampath, Anand; Wraback, Michael. Photodetector with Polarization Induced Electron Filter and Method Thereof. provisional patent filed with USPTO, May, 2013.

Transitions

- The heterogeneous III-Nitride/SiC detector portion of the program has been incorporated into the FY14 mission program and supported using existing Nitride Semiconductor Optoelectronics Team mission funds.
- The GaN/SiC Separate Absorption Multiplication Avalanche Photodiode (SAM-APD) effort, a part of the heterogeneous III-Nitride/SiC detector portion of the program, is a component of a FY15 Coalition Warfare Program proposal in collaboration with Dr. Aime Goad, Edgewood Chemical and Biological Center, and the Republic of Korea. A goal of

the proposal is to incorporate GaN/SiC SAM APDs into the fluorescence channel of light-induced-fluorescence based bio-aerosol sensor.

– ARL Tech Transfer Efforts:

Wraback, Michael; Shen, H. Paul; Metcalfe, Grace D. “Technology Fact Sheet - Creating a More Powerful THZ Source by Engineering Higher Internal Electric Fields”, ARL/RDECOM Technology Fact Sheet for marketing by the ARL Technology Transfer Team, May, 2013.

NO. OF COPIES	ORGANIZATION
1 (PDF)	DEFENSE TECHNICAL INFORMATION CTR DTIC OCA
1 (PDF)	DIRECTOR US ARMY RESEARCH LAB IMAL HRA
1 (PDF)	DIRECTOR US ARMY RESEARCH LAB RDRL CIO LL
1 (PDF)	GOVT PRINTG OFC A MALHOTRA
1 (PDF)	RDRL SEE M A SAMPATH

INTENTIONALLY LEFT BLANK.